Nonlinear Hydrodynamic Models for Heaving Buoy Wave Energy Converters

Giuseppe Giorgi*, Markel Penalba Retes†, John V. Ringwood‡
Centre for Ocean Energy Research
Maynooth University
Maynooth, Co. Kildare, Ireland
Email: *ggiorgi@eeng.nuim.ie, †mpenalba@eeng.nuim.ie, ‡john.ringwood@eeng.nuim.ie

***Abstract*—Numerical models for heaving buoy wave energy converters are a fundamental tool for device design and optimization, power production assessment and model-based controller design. Ideally, models are required to be easy to implement, simple, accurate and computationally efficient. Unfortunately, such features are often conflicting and a compromise has to be reached to define an appropriate model structure.**

A very common choice is to assume a small amplitude of motion and linearize the model. Despite the attractiveness of computational convenience, linear models quickly become inaccurate when large motion occurs. In particular, the implementation of a control strategy, which aims to increase power absorption, enlarges the operational space of the device and significantly enhances the impact of nonlinearities on the model.

There are different possibilities to approach the representation of nonlinearities in heaving point absorbers, each of them characterized by a different level of complexity, computational time requirements and accuracy. This paper compares six different methods: one of them fully-nonlinear (implemented in a computational fluid dynamics environment) and the others based on a linear model with the progressive inclusion of nonlinear restoring force, nonlinear Froude-Krylov force and viscous drag.

***Index Terms*—Wave energy, nonlinear restoring force, nonlinear dynamic Froude-Krylov force, viscous drag, CFD, latching control.**

I. Introduction

Mathematical models for wave energy converters (WECs) typically follow Cummins' equation [1], using hydrodynamic parameters identified, in most cases, using boundary element method (BEM) software such as WAMIT [2]. Most of these models are linear, which are attractive due to their low computational requirements. However, the assumptions under which linear models are valid are restrictive, especially in the case of wave energy devices. The small motion assumption is particularly challenged, since the aim of WECs, especially heaving point absorbers, is to exaggerate the amplitude of motion in order to increase power absorption. As a consequence, significant differences can be observed when comparing linear models to experimental tests [3] or nonlinear models [4], [5].

Numerical models are a crucial tool for wave energy devices design and optimization, power production assessment and model-based controller design. Therefore, models are required to be accurate and computationally acceptable at the same time. Different solutions to improve the linear potential flow model have already been suggested in the literature: nonlinear Froude-Krylov (FK) forces [4], nonlinear radiation and diffraction effects [6], or viscous effects [7]. [8] analyzes the relevance of different nonlinear effects for different wave energy converters, where FK force nonlinearities are identified to be the most important effects for point absorbers. In particular, [4] demonstrates the value of including nonlinear FK forces in controlled heaving point absorbers with a non-uniform cross-sectional area (CSA) which varies with the vertical dimension of the device. Furthermore, [9] shows that nonlinear FK forces are the main component of the total hydrodynamic force.

FK forces are defined as the integral of the static and dynamic incident pressure over the wetted surface of the body. Different approaches to Froude-Krylov force representation have been suggested, which are characterized by different degrees of accuracy, usually inversely proportional to complexity and computational time requirements. This paper intends to compare the following different FK force modelling approaches for heaving point absorbers:

(i) A fully linear model, considering only the mean wetted surface (L),
(ii) A nonlinear static FK force model, focussing on the instantaneous restoring force (NLR),
(iii) A nonlinear static and dynamic FK force model, using the algebraic solution of the pressure integral over the instantaneous wetted surface (NLFKa),
(iv) A nonlinear static and dynamic FK force model, using a discretized geometry and a re-meshing routine to determine the instantaneous wetted surface (NLFKr).

Furthermore, in order to study the relative importance of nonlinear FK forces, and to evaluate the accuracy of the results, other nonlinear effects are considered:

(v) An algebraic nonlinear static and dynamic FK forces model with a viscous drag term (NLFKaD),
(vi) A fully-nonlinear model, using a computational fluid dynamics software (CFD).

Models (i) to (vi) are implemented to simulate the response of two heaving point absorbers with regular and irregular wave excitation under uncontrolled and controlled conditions. The geometries under study are a sphere and a cone which, due to their non-uniform CSA, are likely to show significant nonlinearities and, in the case of the cone, asymmetry of the response around the equilibrium point. The chosen control strategy is latching [10], which enlarges the amplitude of

motion, enhancing the relative displacement of the device (in relation to the free-surface elevation), which, in turn, magnifies the instantaneous wetted surface variations and, consequently, the relevance of nonlinear FK forces. Latching is chosen due to its simplicity, prevalence in the literature, and the fact that it induces significantly exaggerated motion under controlled conditions.

The purpose of the paper is to compare the performance of models (i) to (vi) in order to discuss the value of increasing the models complexity in relation to accuracy and computational cost margins.

The reminder of the paper is organized as follows: Section II presents the different hydrodynamic models in detail. Case studies are analyzed in Section III and results are given in Section IV. A discussion of the results is presented in Section V and some conclusions and final remarks are presented in Section VI.

II. Hydrodynamic models

Models (i) to (v), as described in section I, are based on a common theoretical background, which develops under the assumption of an inviscid fluid and irrotational and incompressible incident flow. As a result, the dynamics of the floating system can be described by Newton's second law:

$$m\ddot{\mathbf{z}}(t) = \mathbf{F}_g - \iint_{S(t)} P(t)\ \mathbf{n}\ dS + \mathbf{F}_{PTO}(t) \tag{1}$$

where m is the mass of the floater, $\mathbf{z}$ the vertical displacement of the body from its hydrostatic equilibrium position, $\mathbf{F_g}$ the gravity force, S the submerged wetted surface, P the pressure, $\mathbf{n}$ the vector normal to the surface and $\mathbf{F}_{PTO}$ the power take-off (PTO) force.

Applying Bernoulli's equation to the incident flow [11], the formulation of the pressure P is obtained as:

$$P(t) = -\rho g z(t) - \rho\frac{\partial\phi(t)}{\partial t} - \rho\frac{|\nabla\phi(t)|^2}{2} \tag{2}$$

where ρ is the density of the water, g the acceleration due to gravity, $P_{st} = -\rho g z$ the hydrostatic pressure and ϕ the potential flow, which, based on linear wave theory, is the sum of the undisturbed incident flow potential ϕ_I, the diffraction potential ϕ_D and the radiation potential ϕ_R:

$$\phi(t) = \phi_I(t) + \phi_D(t) + \phi_R(t) \tag{3}$$

Combining equations (1) to (3), the following hydrodynamic forces are defined:

- $\mathbf{F}_{FK_{st}}$ is the static Froude-Krylov force, given as the balance between the gravity force and the force due to the static pressure P_{st}:

$$\mathbf{F}_{FK_{st}}(t) = \mathbf{F}_g - \iint_{S(t)} P_{st}(t)\ \mathbf{n}\ dS \tag{4}$$

- $\mathbf{F}_{FK_{dy}}$ is the dynamic Froude-Krylov force:

$$\mathbf{F}_{FK_{dy}}(t) = -\iint_{S(t)} P_{dy}(t)\ \mathbf{n}\ dS, \tag{5}$$

where $P_{dy} = -\rho\frac{\partial\phi_I}{\partial t} - \rho\frac{|\nabla\phi_I|^2}{2}$ is the dynamic pressure.

- $\mathbf{F}_D$ is the diffraction force:

$$\mathbf{F}_D(t) = -\iint_{S(t)} P_D(t)\ \mathbf{n}\ dS, \tag{6}$$

where $P_D = -\rho\frac{\partial\phi_D}{\partial t} - \rho\frac{|\nabla\phi_D|^2}{2}$ is the diffraction pressure.

- $\mathbf{F}_R$ is the radiation force:

$$\mathbf{F}_R(t) = -\iint_{S(t)} P_R(t)\ \mathbf{n}\ dS, \tag{7}$$

where $P_R = -\rho\frac{\partial\phi_R}{\partial t} - \rho\frac{|\nabla\phi_R|^2}{2}$ is the radiation pressure.

The time-dependance annotation will be omitted for brevity hereafter. Using equations (4) to (7), (1) can be rewritten as:

$$m\ddot{\mathbf{z}} = \mathbf{F}_{FK_{st}} + \mathbf{F}_{FK_{dy}} + \mathbf{F}_D + \mathbf{F}_R + \mathbf{F}_{PTO} \tag{8}$$

Several sources of nonlinearity are present in equations (1) to (8), namely the quadratic terms and the possibly nonlinear incident potential flow in Bernoulli's equation (2) and the instantaneous variation of the wetted surface. Quadratic terms in equation (2) can be neglected for heaving point absorbers, as shown by [12], and only linear waves are considered, which cover the vast majority of the waves in the power production region.

The following subsections detail each of the models (i) to (vi).

A. Linear model

For linear model (i), the potential problem is linearized and solved around the equilibrium position, hence small motion is assumed and the mean wetted surface S_M is considered. Equation (8) is now given as:

$$\begin{aligned} m\ddot{\mathbf{z}} = \underbrace{-K_H\mathbf{z}}_{\mathbf{F}_{FK_{st}}} - \underbrace{\int_{-\infty}^{\infty} K_{ex}(t-\tau)\ \eta(\tau)\ d\tau}_{\mathbf{F}_{ex}=\mathbf{F}_{FK_{dy}}+\mathbf{F}_D} + \\ \underbrace{-\mu_\infty\ddot{\mathbf{z}} - \int_{-\infty}^{\infty} K_R(t-\tau)\ \dot{\mathbf{z}}(\tau)\ d\tau}_{\mathbf{F}_R} - \mathbf{F}_{PTO} \end{aligned} \tag{9}$$

where:

- $\mathbf{F}_{FK_{st}}$ is described by the linear hydrostatic stiffness K_H;
- $\mathbf{F}_{ex}$ is the excitation force and is represented by the convolution product between the excitation impulse-response function (IRF) K_{ex} and the free-surface elevation η;
- $\mathbf{F}_R$ is represented by the infinite added mass μ_∞ and the convolution product between the radiation IRF K_R and the velocity $\dot{\mathbf{z}}$, based on Cummins' equation [1];

The added mass and the impulse response functions are calculated by the frequency domain BEM software WAMIT [2].

The computationally expensive radiation convolution product is replaced by its state space representation, as shown in [13].

B. Nonlinear restoring force model

For the nonlinear restoring force model (ii), as shown in Fig. 1, the $\mathbf{F}_{FK_{st}}$ integral in equation (4) is computed over the instantaneous wetted surface S, which can be described as the closed surface S_c minus the horizontal surface S_{WP}, as shown in [14]. S_{WP} is defined as the intersection between the body and the horizontal plane at the free surface elevation η. Consequently, $\mathbf{F}_{FK_{st}}$ can be computed as follows:

$$\mathbf{F}_{FK_{st}} = \mathbf{F}_g - \left(\iint_{S_c} P_{st}\ \mathbf{n}\ dS - \iint_{S_{WP}} P_{st}\ \mathbf{n}\ dS \right) \tag{10}$$

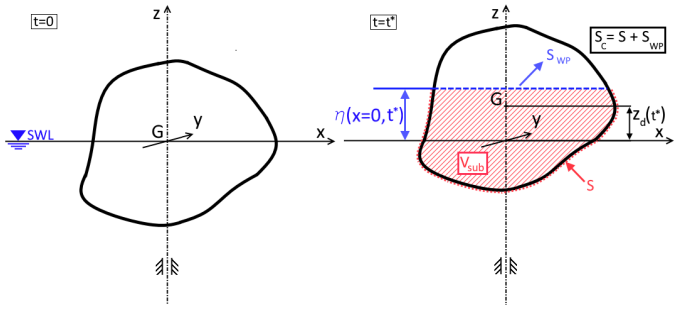

Fig. 1. Generic heaving device: the figure on the left shows the rest position, with the center of gravity G at the still water level (SWL); the figure on the right shows the free surface elevation η and the device displacement z_d after a time t^*. The closed surface S_c surrounds the submerged volume V_{sub}, which is upper limited by the water plane surface S_{WP}.

Applying Gauss's divergence theorem to the integral over the closed surface S_c, equation (10) becomes:

$$\mathbf{F}_{FK_{st}} = \mathbf{F}_g + (\rho g V_{sub} - \rho g \eta A_{WP})\,\mathbf{k} \tag{11}$$

where V_{sub} is the submerged volume enclosed by S_c, A_{WP} is the area of S_{WP} and $\mathbf{k}$ is the vertical unity vector.

Since the instantaneous wetted surface is taken into account, it is possible to evaluate when the relative displacement between the vertical motion of the floater and the free surface elevation exceeds the vertical dimensions of the floater itself, i.e. when the floater is completely out of the water. In such an unrealistic situation, the fluid force is absent; therefore, the excitation force is set to zero.

The nonlinear restoring force method is applicable to any geometry since it is always possible to obtain, either analytically or through a CAD software, the variations in volume and CSA with the vertical coordinate.

C. Nonlinear Froude-Krylov model - algebraic approach

For the algebraic nonlinear FK model (iii), the FK integrals in equation (4) and (5) are solved algebraically over the instantaneous wetted surface. Static and dynamic pressure are obtained by applying Airy's wave theory for deep water waves:

$$P(x,z,t) = \rho g a e^{\chi z} \cos(\omega t - \chi x) - \rho g z \tag{12}$$

where x is the direction of wave propagation, a is the wave amplitude, χ the wave number and ω the wave frequency.

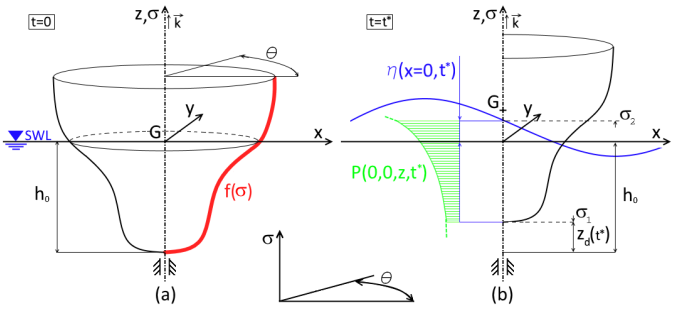

Fig. 2. Axisymmetric heaving device with generic profile $f(\sigma)$: the Fig. on the left shows the rest position, with the center of gravity G at the still water level (SWL) and draft h_0; the figure on the right shows the free surface elevation η and the device displacement z_d after a time t^*. The pressure is integrated over the surface between σ_1 and σ_2 [15].

As shown in detail in [15], an algebraic solution is achievable for any axisymmetric heaving point absorber, such as that shown in Fig. 2, which can be described by parametric cylindrical coordinates $[\sigma, \theta]$ as:

$$\begin{cases} x(\sigma,\theta) = f(\sigma)\cos\theta \\ y(\sigma,\theta) = f(\sigma)\sin\theta \\ z(\sigma,\theta) = \sigma \end{cases} \quad , \quad \sigma \in [\sigma_1, \sigma_2] \wedge \theta \in [0, 2\pi) \tag{13}$$

Referring to the notation of Fig. 2, the resulting FK force in heave is computed as follows:

$$\mathbf{F}_{FK_z} = \mathbf{F}_g - \int_0^{2\pi} \int_{\sigma_1}^{\sigma_2} P(x(\sigma,\theta), z(\sigma,\theta), t) f'(\sigma) f(\sigma) \mathbf{k} d\sigma d\theta \tag{14}$$

where the limits of integration which define the instantaneous wetted surface are $\sigma_1 = z_d - h_0$ and $\sigma_2 = \eta$.

The algebraic solution of (14) is straightforward and it is easy to implement in the simulation model. However, it can only be implemented for axisymmetric bodies.

As the dynamic FK force is computed nonlinearly (and separately), the diffraction part of the excitation force is computed through the diffraction IRF K_D:

$$\mathbf{F}_D = -\int_{-\infty}^{\infty} K_D(t-\tau)\ \eta(\tau)\ d\tau \tag{15}$$

Similarly to Section II-B, as the relative displacement exceeds the vertical dimension of the floater, the diffraction force is set to zero.

D. Nonlinear Froude-Krylov model - re-meshing approach

For the re-meshing nonlinear FK force model (iv), the integrals in equation (4) and (5) are solved over the instantaneous wetted surface, as in the case of model (iii) in Section II-C. However, in this method, the geometry is discretized into small

plane panels, which allows the computation of FK forces for any shape and not only for axisymmetric bodies, as in Section II-C. On the other hand, the definition of the instantaneous wetted surface requires a computationally expensive re-meshing routine which redefines the panels every time step as the free surface elevation changes. Furthermore, the complexity of this method requires a significant programming effort of implementation. A detailed description of the re-meshing approach is given in [6].

E. Nonlinear Froude-Krylov and viscous drag model

For the nonlinear algebraic FK force and viscous drag model (v), Froude-Krylov forces are modeled as in Section II-C while a viscous drag term is included in the model following the Morrison equation [**?**]:

$$\mathbf{F}_{vis} = -\frac{1}{2}\rho\, C_d A_d \left|\mathbf{V} - \mathbf{V}_0\right| (\mathbf{V} - \mathbf{V}_0), \tag{16}$$

where C_d is the drag coefficient, A_d is the characteristic area, $\mathbf{V}$ is the velocity of the floater and $\mathbf{V}_0$ is the undisturbed flow velocity. Note that the characteristic area is the projection of the instantaneous wetted surface onto the plane normal to the flow.

Notwithstanding the simplicity of the viscous model in (16), the definition of the drag coefficient C_d is not straightforward. Ideally, experimental tests can be used to identify C_d, as in [16]. Nevertheless, in most cases, accessing wave tank facilities is costly and time consuming and having a prototype device to test is not always possible. Such problems may be overcome by performing the identification of C_d in a numerical wave tank using CFD simulations, as in [17].

On the other hand, if simple geometries are considered, it is possible to define C_d *a priori* based on established theoretical or tabulated knowledge, rather than using experimental or numerical tank tests. In the case of heaving floating buoys, the Keulegan-Carpenter number KC can be used, which is the dimensionless quantity defined as the ratio between drag and inertia forces acting on a body in an oscillatory fluid flow [18]. In the case of sinusoidal motion, the KC number can be computed as:

$$KC = 2\pi\frac{A}{L_c} \tag{17}$$

where A is the amplitude of motion and L_c is the characteristic length scale. For the case of the sphere in Fig. 3, the amplitude of motion is likely to be of the same order of magnitude as the characteristic length (the diameter), resulting in a Keulegan-Carpenter number KC of about 2π and, according to [19], a drag coefficient C_d equal to 1.

F. Fully-nonlinear CFD model

The fully-nonlinear model (vi) is implemented in a numerical wave tank (NWT) using the open-source CFD software OpenFOAM [20]. The fluid dynamics are described by a set of differential equations known as Navier-Stokes equations [21] under the incompressibility assumption:

$$\nabla \cdot \mathbf{u} = 0 \tag{18}$$

$$\rho\frac{\partial \mathbf{u}}{\partial t} + \rho\mathbf{u}\cdot\nabla\mathbf{u} = -\nabla P + \nabla\cdot\mathbf{T} + \rho\mathbf{g} \tag{19}$$

where $\mathbf{u}$ is the fluid velocity and $\mathbf{T}$ is the stress deviator, given by.

$$\mathbf{T} = \mu[\nabla\mathbf{u} + (\nabla\mathbf{u})^T] \tag{20}$$

where μ is the dynamic viscosity.

All the details about the definition of the computational domain and the boundary conditions are given in [5].

The main benefit of this modelling approach is its high fidelity, since it includes all nonlinear effects. Therefore, it is taken as a fidelity benchmark to evaluate the results obtained with the other models.

However, CFD models are very complex and time demanding. Besides a computational time several orders of magnitude higher than boundary-element models, a significant effort and experience is required to correctly set up NWT dimensions, mesh and parameters, often relying on an exhaustive trial and error process.

III. Case studies

Most of the main heaving point absorbers currently under development are either cylindrical devices - with a conical bottom [22] - or sphere-type devices [23], [24]. Since nonlinear FK forces in cylinders are insignificant, as shown in [4], due to the uniform CSA, other devices, such as a sphere and a cone, are considered. Inspired by the Wavestar device [23], the chosen sphere has a radius of 2.5 m and its center of gravity G is at the still water level (SWL), as shown in Fig. 3. However, since the CSA of the sphere changes symmetrically with respect to the still water level, the motion is expected to be significantly symmetric, even for a nonlinear model. In order to show the ability of nonlinear models to capture the dynamics of asymmetric shapes, a cone is considered as well. The dimensions of the cone, as shown in Fig. 3, have been chosen so that draft and radius at the SWL are the same as for the sphere.

The devices are constrained to move in heave only and are tethered to the seabed with a linear damper acting as a PTO, in combination with a latching mechanism.

In order to focus only on nonlinearities caused by FK forces, linear waves based on Airy's theory are used, assuming a small steepness (H_w/λ) of 0.018 [25], defined as the ratio between the wave height H_w and wave length λ. Furthermore, the devices are assumed to operate in deep water conditions. Initially, monochromatic waves are considered in order to analyze the response of the device at each different frequency independently, with wave periods T_w chosen to cover the common sea states experienced by a point absorber [26]. Since FK nonlinearities are caused by changes in the instantaneous wetted surface, which depends on the intersection between the free surface elevation and the body position, the higher

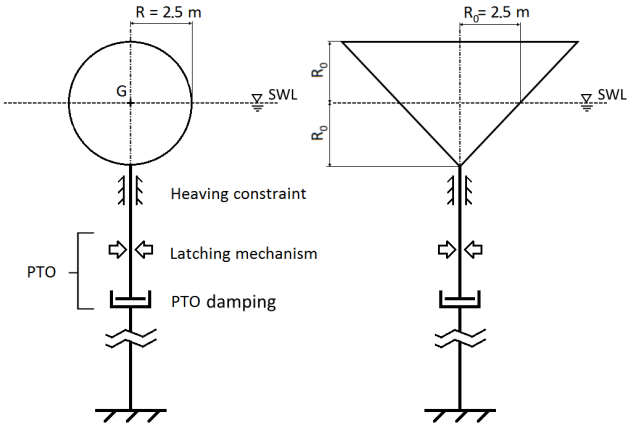

Fig. 3. Case study: a sphere with radius R and with its center of gravity G at the SWL and a cone with draft and radius at the SWL, with $R_0 = R$. Both devices are constrained to move in heave only and deep water conditions are assumed. The PTO system is composed of a linear damper and a latching mechanism.

TABLE I
REGULAR SEA STATES: LINEAR MONOCHROMATIC DEEP WATER WAVES ACCORDING TO AIRY'S THEORY.

Wave steepness	H_w/λ	0.018						
Wave period [s]	T_w	**4**	**5**	**6**	**7**	**8**	**9**	**10**
Wave height [m]	H_w	0.44	0.69	1	1.36	1.78	2.25	2.78

the wave steepness, the higher the relevance of FK nonlinearities. Therefore, the highest steepness allowed in linear wave theory [25] has been chosen because it generates the most significant nonlinear response. Moreover, the same steepness is considered for all wave periods in order to have the same (scaled) wave profile and, consequently, a fair comparison. The resulting regular sea states are summarized in table I.

In addition to regular waves, an irregular sea state is considered as well, using a Jonswap spectrum with significant wave height H_s 1 m, peak period T_p 6 s, γ equal to 5 and phases randomly chosen [19]. The simulations are 400 seconds long in total, but the first half of the simulated response is discarded, in order to remove any transient effect.

The relevance of FK nonlinearities strongly depends on the relative amplitude of motion of the floater with respect to the free surface elevation. Therefore, latching control has been implemented in order to enlarge the displacement of the device, avoiding the WEC acting as a wave-follower. A latching control strategy consists of locking (latching) the device motion at its displacement extrema (when the device velocity is zero) and subsequently releasing it (unlatching) in order to bring the system velocity into phase with the excitation force. Following the zero-threshold unlatching criteria [27], the device is unlatched as soon as the excitation force changes sign. The PTO damping coefficient is set equal to the radiation damping coefficient at the wave period for regular waves, and at the peak period for irregular waves.

Note that the configuration of the devices, the sea state conditions and the control strategy is the same for all the numerical models.

Finally, a single CFD simulation has been carried out for a harmonic wave of period $T_w = 6$ s because of the high computational time required to set up the numerical wave tank parameters and complete the simulation for all wave periods. Details concerning the mesh of the numerical domain and the boundary conditions are given in [5].

IV. RESULTS

As shown in Section I, six models are considered: linear model L (i), nonlinear restoring force model NLR (ii), algebraic nonlinear FK force model NLFKa (iii), re-meshing nonlinear FK force model NLFKr (iv), nonlinear FK and viscous drag force model NLFKaD (v) and CFD model (vi). Since models (iii) and (iv) give the same results [15], and differ only in computational time, they will be jointly referred to as model (iii-iv) in the presentation of the results.

Initially, a sphere and a cone are considered, in order to show the ability of the models to capture the dynamics of asymmetric devices. For the modeling comparison study, only the sphere is considered and models (i) to (vi) are compared in terms of accuracy and computational time requirements.

FK forces depend on the wetted surface of the floater, therefore nonlinearities arise if the CSA of the device is not uniform along the direction of motion. Linear model (i) considers the constant mean wetted surface, therefore the motion will always be symmetric around the equilibrium, irrespective of the specific geometry of the device. On the contrary, nonlinear models (ii) and (iii-iv) take into account the instantaneous wetted surface of the floater, and account for the CSA variations of the body, which can lead to an asymmetric motion. Considering the sphere and the cone presented in Section III, Fig. 4 shows the asymmetry of the motion, defined as the absolute value of the ratio between extrema of motion, where a value greater than one means a motion larger in the positive direction.

As expected, the linear model (i) generates symmetric motion for both geometries. In the case of the sphere, which is symmetric with respect to the SWL, the motion is symmetric even for model (ii), since the static pressure $P_{st} = -\rho g z$ changes symmetrically around the SWL. On the other hand, a small asymmetric behavior appears in models (iii-iv) due to the asymmetric profile of the dynamic pressure, which varies with an exponential profile as shown in (12). Conversely, in the case of the cone, which has a strongly asymmetric geometry with respect to the SWL, both models (ii) and (iii-iv) show an asymmetric motion, which is much more pronounced than for the sphere.

The relevance of nonlinearities depends on the amplitude of motion, which is significantly enlarged by the action of the controller. In particular, nonlinearities in FK forces are enhanced by the relative displacement between the body and the free surface elevation ($\eta - z$), while viscous drag effects depend on the velocity of the floater. Fig. 5 shows an example

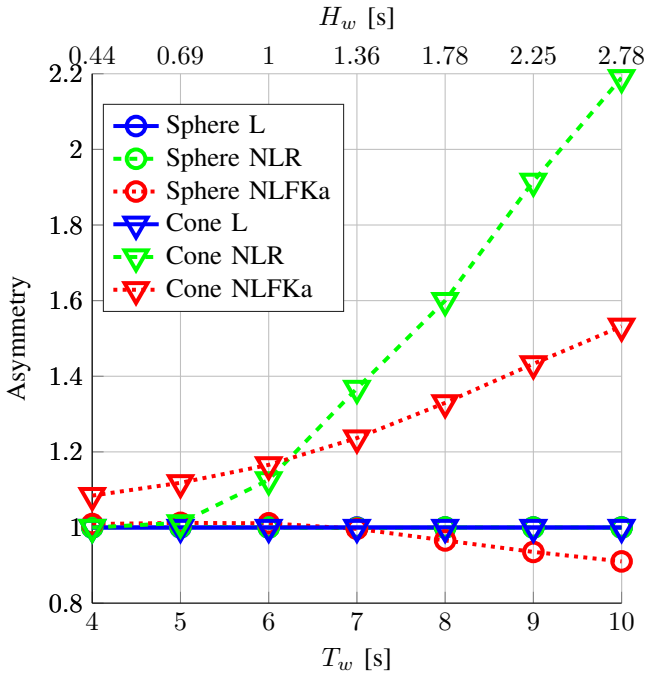

Fig. 4. Asymmetry, defined as the absolute value of the ratio between maximum and minimum displacement, for the sphere and the cone using different Froude-Krylov force representations under controlled conditions.

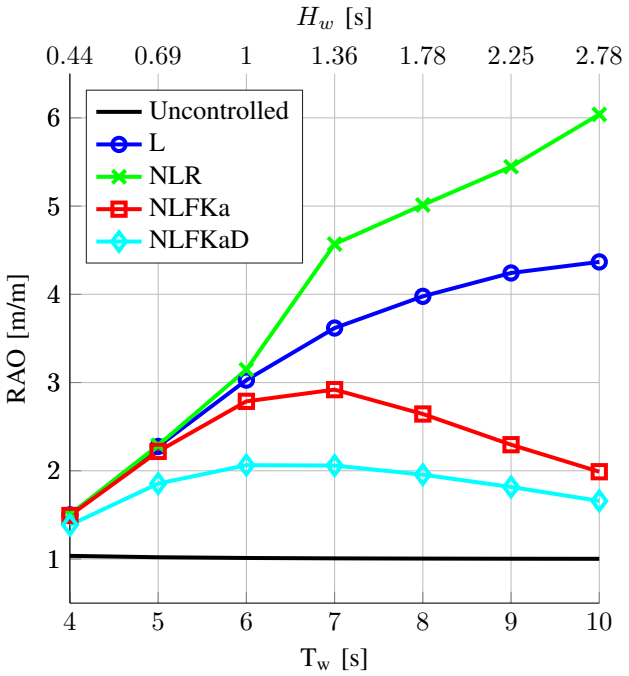

Fig. 6. Response amplitude operator (RAO) for the sphere, with and without control applied.

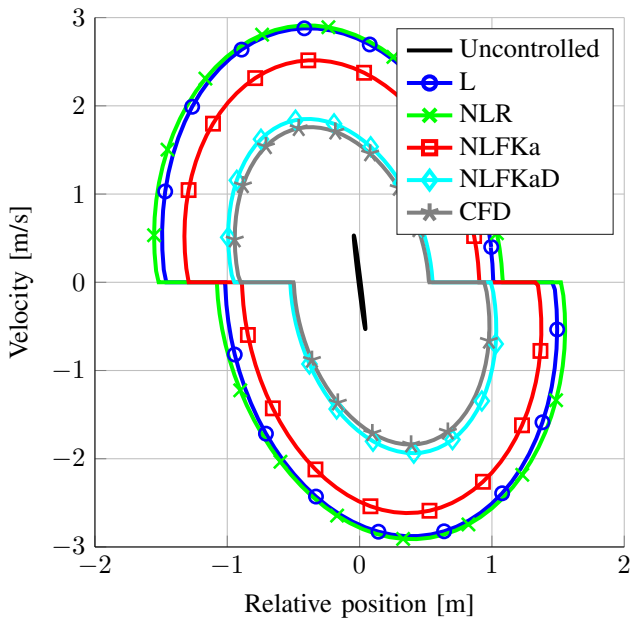

Fig. 5. Operational space for the sphere, with and without control applied, using a regular wave of period T_w 6 s and H_w 1 m.

of the velocity-relative displacement operational space for the sphere, with and without latching control applied.

Only one trace for the uncontrolled case is drawn since all the models effectively overlap. Nonlinearities are indeed negligible as the very small relative displacement and velocity indicate that the floater is behaving as a wave follower. Conversely, the latching control strategy significantly increase the amplitude of the motion compared to the linear case, so nonlinear effects become considerable.

In addition to the controller action, nonlinearities depend on the wave period and height, as shown by the response amplitude operators (RAOs) in Figure 6.

In uncontrolled conditions, the device behaves as a wave follower since the RAO is effectively unity for all wave periods, as the natural period of the device is smaller than 4 s. On the other hand, under controlled conditions, nonlinearities in FK force become significant for large waves ($T_w \geq 7$ s).

In model (ii), the inclusion of only a nonlinear restoring force has the effect of increasing the amplitude of motion with respect to the linear case. Indeed, in the linear case the restoring force is computed as if the CSA was constant, therefore considering the volume varying as if it was a cylinder. Conversely, since the CSA is decreasing as the body moves away from the equilibrium position, the actual variation of the volume of the sphere is smaller than for the linear model; therefore, a smaller restoring force is expected and, as a consequence, a larger amplitude of motion ensues. Moreover, the magnitude of the nonlinear restoring force has an upper limit equal to the gravity force (when the body is completely out of the water or completely submerged) while, in the linear case, the restoring force is unbounded and directly proportional to the displacement.

On the other hand, considering both nonlinear static and dynamic FK forces as in models (iii-iv), the amplitude of motion is drastically reduced at large periods compared to the linear case, suggesting that the variation in the instantaneous

wetted surface causes the nonlinear dynamic FK force to be much smaller than in the linear case. Furthermore, the reduction of the dynamic FK force is larger than the reduction of the static FK force.

Finally, model (v) highlights the dissipative effect of drag, which diminishes the response of the device at every wave period.

It is important to compare the relative importance of nonlinear FK force and viscous drag at different periods. Models (iii-iv), which include only a nonlinear FK force, show a RAO that is diverging from the linear RAO as the wave becomes larger, demonstrating the increasing importance of FK nonlinearities with increasing wave amplitude. On the other hand, the difference between the RAOs of models (v) and (iii-iv) increases until a wave period of 7 s and then decreases. Since model (v) differs from models (iii-iv) only in relation to the viscous drag term, it is possible to conclude that, for small wave periods, viscous drag effects are more important than FK nonlinearities. On the other hand, FK nonlinearities are more important than viscous drag for large wave periods.

In addition to the amplitude of motion, it is interesting to consider the relative displacement between the device and the free surface elevation, as shown in Fig. 7. Without control, the relative displacement is effectively null, so the device behaves as a wave follower. Under controlled conditions, and for small periods, the relative displacement is small, so the differences between linear and nonlinear models are small. For larger wave periods, the relative displacement increases and the relative displacement curves diverge.

Furthermore, if the relative displacement exceeds the physical limit of the radius of the sphere, it means that the device is (unrealistically) out of the water. While models (i) and (ii) cross this physical limit after a wave period of 6 s, nonlinear models (iii-iv) and (v) remains below it for the full range of wave periods.

Since one of the main purposes of a mathematical WEC model is power production assessment, Fig. 8 shows the power produced by the device according to the different models. The general trend is similar to the RAO trend shown in Fig. 6. Therefore, power production predictions based on models (i) and (ii) are significantly overestimated compared to models (iii-v).

The results presented so far have been obtained using models (ii) to (v), which include different nonlinear terms compared to the same linear model (i) based on BEM theory. A different (fully-nonlinear) approach is followed by the CFD model (vi), which has been used to simulate the motion for a regular wave of period 6 s and height 1 m. CFD is a useful tool to produce graphical representations of the nonlinear wave-body interactions. Figures 9(a) and 9(b) show, respectively, the peak and bottom position of the floater without control, while Figures 9(c) and 9(d) show, respectively, the peak and bottom position at the unlatching instant.

It is evident that, without control, the center of the body is approximately at the free surface elevation height; therefore, the floater is behaving as a wave follower and nonlinearities

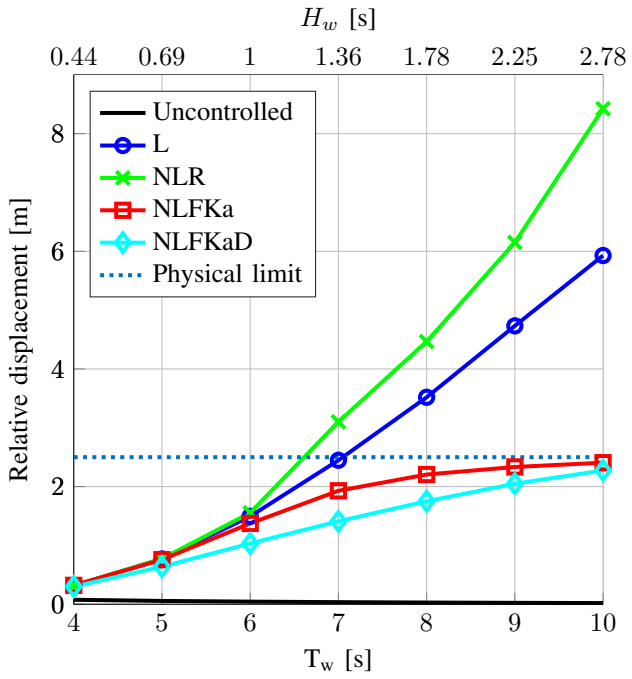

Fig. 7. Relative displacement between the sphere and the surface elevation, with and without control applied.

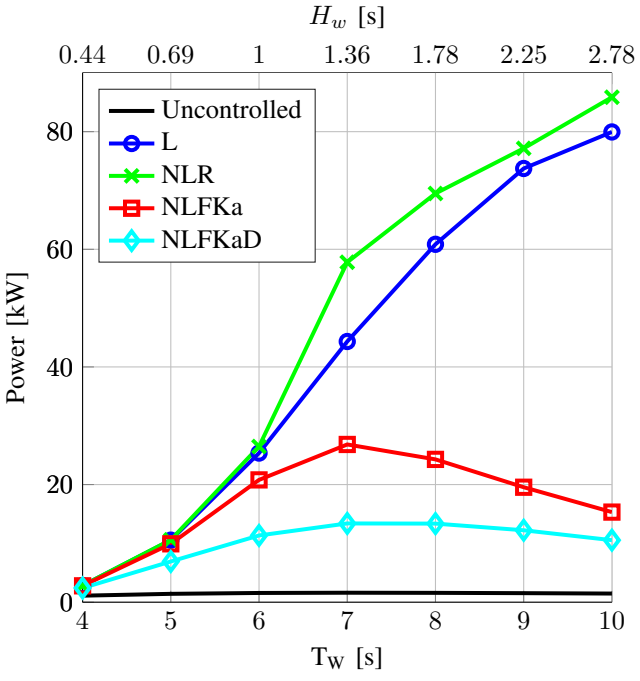

Fig. 8. Power absorption for the sphere, with and without control applied.

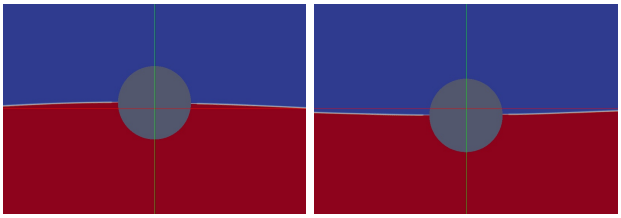

(a) Top position without control. (b) Bottom position without control.

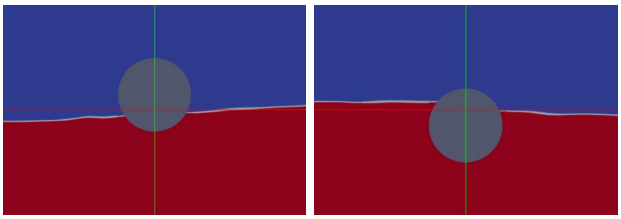

(c) Top position with control at the unlatching instant. (d) Bottom position with control at the unlatching instant.

Fig. 9. Screen-shots of CFD simulations for a sphere, using a regular wave of period T_w 6 s and H_w 1 m.

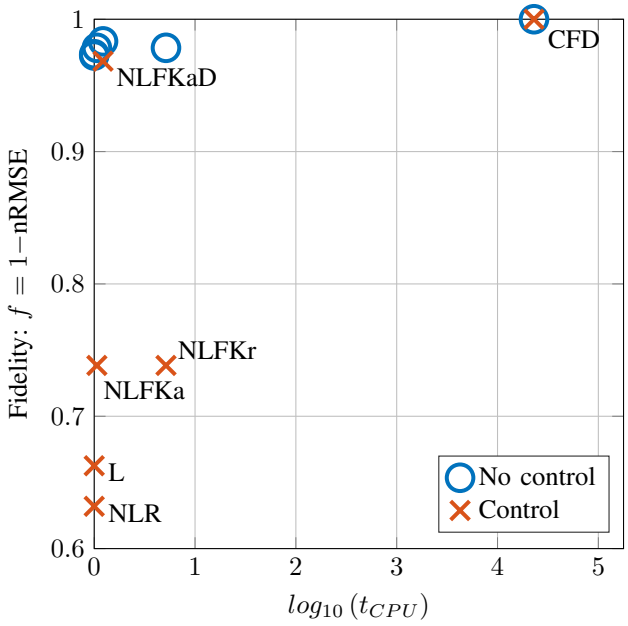

Fig. 10. Normalized computational time versus fidelity, defined as in (21), with and without control, using a regular wave of period T_w 6 s and H_w 1 m..

are negligible. On the other hand, when control is applied, larger amplitude of motion and significant variations in instantaneous wetted surface appear.

CFD is based on the resolution of the fully-nonlinear Navier-Stokes equations, so its results are taken as a fidelity benchmark and used to evaluate the accuracy of the other models. Regarding the displacement of the body, a fidelity index f_j is computed, following the transient, over one wave period T_w as the unity minus the normalized root mean squared error (nRMSE) between the displacement computed in CFD $z_{(vi)}$ and the displacement computed with each model z_j:

$$f_j = 1 - \frac{1}{\overline{z_{(vi)}}} \sqrt{\frac{\sum_{t_i=t_0}^{t_0+T_w} \left(z_{(vi)}(t_i) - z_j(t_i)\right)^2}{n}} \qquad (21)$$

where n is the number of time samples, j stands for models (i) to (vi) and $\overline{z_{(vi)}}$ is the difference between the maximum and minimum values of the displacement in the CFD model.

While the CFD model has, by definition, the highest fidelity, it requires a computational time several orders of magnitude greater than the other models. Therefore, a fair comparison between the models needs to consider both the fidelity f and the computational time t_{CPU}, which are both shown in Fig. 10 under uncontrolled and controlled conditions. The numerical values for the controlled case are shown in Tab. II. The computational time is normalized against the linear model. It is important to remark that the values of fidelity shown in Fig. 10 and Tab. II refer only to the regular wave with period $T_w = 6$ s and height $H_w = 1$ m. On the one hand, the normalized computational times have general validity since they are approximately insensitive to the wave characteristics; on the other hand, the differences between the response of

TABLE II

FIDELITY AND NORMALIZED COMPUTATIONAL TIME UNDER CONTROLLED CONDITIONS, USING A REGULAR WAVE OF PERIOD T_w 6 S AND H_w 1 M.

	(i) L	(ii) NLR	(iii) NLFKa	(iv) NLFKr	(v) NLFKaD	(vi) CFD
f	0.66	0.63	0.74	0.74	0.97	1
t_{CPU}	1	1.09	1.26	5.15	1.35	23000

models (i) to (v), so the relative difference in their fidelity, is strongly related to the wave conditions, as previously shown in Figures from 6 to 8.

The uncontrolled case has been included in order to certify that the CFD model setup is correct and produces results consistent with the other models. Since, without control, it has been shown that nonlinearities are effectively negligible, the fidelity index is close to unity for all the models.

On the other hand, major differences are found under controlled conditions. The most evident result is the significantly high fidelity of model (v) at a drastically lower computational time compared to model (vi), showing that the combination of nonlinear FK and viscous drag covers most of the nonlinearities present in a heaving sphere. Furthermore, there is a significant improvement in fidelity with respect to the linear model.

Models (iii) and (iv) follow two different approaches to nonlinear FK forces representation, which are equivalent in terms of accuracy but significantly different in computational time requirements. The improvement in accuracy of models (iii-iv), with respect to the linear model, is not as dramatic as in model (v), mainly because at the wave period $T_w = 6$ s viscous effects are more important than FK nonlinearities, as shown in Fig. 6. On the other hand, since the importance

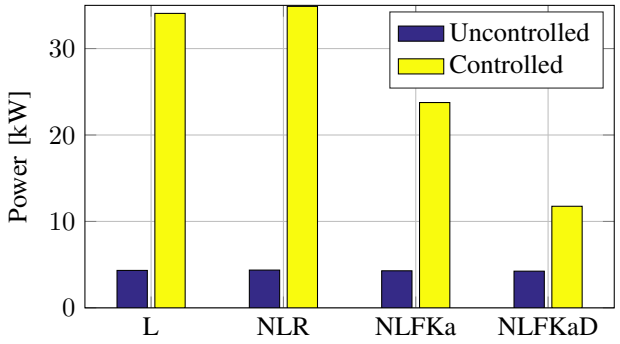

Fig. 11. Power absorbed using an irregular sea state based on the Jonswap spectrum with significant wave height $H_s = 1$ m, peak period $T_p = 6$ s, $\gamma = 5$, with phases randomly chosen.

of nonlinear FK forces increases with the wave periods, the fidelity of models (iii-iv) is expected to be much higher than the linear model, when larger waves are considered.

Finally, model (ii) shows a lower accuracy than the linear model, suggesting that it is not useful to consider nonlinear static FK force (nonlinear restoring force) and linear dynamic FK force concurrently. Indeed, the static and dynamic parts of the incident pressure in (12) have opposite signs and partially balance each other; therefore, it is preferable to integrate the total pressure (both static and dynamic parts) either over the mean wetted surface (model (i)) or over the instantaneous wetted surface (models (iii-iv)).

Following the analysis of the response with regular waves, an irregular sea state is considered, based on the Jonswap spectrum with significant wave height $H_s = 1$ m, peak period $T_p = 6$ s, $\gamma = 5$, with phases randomly chosen. The power production for models (i) to (v), with and without control, is shown in Fig. 11.

Consistent with the results obtained for regular waves in Fig. 8, the power produced for the uncontrolled case is effectively constant regardless of which model is used, confirming the negligible relevance of nonlinearities. On the contrary, as the controller enlarges the amplitude of motion and the power absorption, differences arise between model responses. While model (ii) is slightly overestimating the power extracted, models (iii-iv) and (v) show a conspicuous amount of power lost due to nonlinear FK forces and viscous drag.

V. Discussion

The choice of an appropriate mathematical model for a heaving point absorber is not straightforward and needs to take account of many different factors: the shape of the device, wave conditions, presence/absence of control, complexity and computational time requirements and the desired accuracy.

Choosing the modeling approach determines what nonlinearities need to be considered in the model and how they are represented. Six different modeling options have been studied and compared in this paper, one of them based on CFD and the others based on BEM theory with the progressive inclusion of nonlinear restoring force, nonlinear FK force and viscous drag.

TABLE III
Qualitative comparison of the models considering flexibility, complexity, computational time requirements and fidelity, where 5 stands for a high "value" of each parameter. Color code: very negative, negative, medium, positive, very positive.

	(i) L	(ii) NLR	(iii) NLFKa	(iv) NLFKr	(v) NLFKaD	(vi) CFD
Flexibility	5	5	2	5	1	5
Complexity	1	2	2	5	3	5
Computation	1	1	1	4	2	5
Fidelity	2	1	3	3	4	5

The six different models have advantages and disadvantages, so the following criteria can be used to guide the choice of the compromise that best suits one's needs and priorities:

- Flexibility: it refers to the possibility or the difficulty of applying the method to a particular device due to its geometry.
- Complexity: it refers to the effort and time needed to implement the method.
- Computation: it refers to the computational time needed to perform the simulation.
- Fidelity: it refers to the accuracy of the results of the simulation.

A first important result is that under uncontrolled conditions, no nonlinear effect is significantly excited; therefore, there is no clear advantage in using nonlinear models in such a case. Nevertheless, in wave energy, a control strategy is normally required in order to increase power absorption, so the inclusion of nonlinearities is likely to be necessary.

Tab. III shows a qualitative comparison of the models considered in this paper according to the criteria of flexibility, complexity, computation and fidelity (under controlled conditions). Numbers from 1 to 5 are used, where 5 stands for a "high" value of each parameter. Moreover, a color code has been used, as explained in the caption, since a high value for flexibility and fidelity is a positive feature as opposed to a negative feature for complexity and computation and vice versa.

The linear model (i) is very fast to compute, easy to implement and is applicable to any device geometry, since a common BEM software can be used to obtain the hydrodynamic coefficients. Nevertheless, low accuracy is expected.

The nonlinear restoring model (ii) requires the definition of how the volume and CSA varies in the vertical direction, which is straightforward for simple geometries and is even possible for complex geometries, if CAD software is used. On the other hand, for the sphere considered in this paper, the results are less accurate than for the linear model.

The algebraic nonlinear FK model (iii) is applicable only to axisymmetric devices since it requires the algebraic solution of the pressure integral. On the other hand, the algebraic solution allows the computational time to remain approximately the

same as in the linear model. The computation of the nonlinear FK forces improves the model fidelity significantly.

Nonlinear FK forces can be alternatively computed using a re-meshing routine approach as in model (iv), leading to the same gains in fidelity of model (iii). On the other hand, it is necessary to code complex software which discretizes the geometry of the device and, in real-time, re-meshes the instantaneous wetted surface, which is computationally very expensive. In addition, an advantage of model (iv) over model (iii) is that any geometry can be simulated, regardless of the complexity of its shape.

Model (v) essentially comprises model (iii) plus a viscous drag term, which considerably increases the fidelity at a low computational cost. Nevertheless, the viscous drag coefficient needs to be determined; while it is known a priori for simple geometries, experiments in real or numerical wave tanks are required for complex geometries.

Finally, model (vi) is the most accurate but its computational time is several orders of magnitude larger than the other models. Moreover, considerable experience and effort is needed to set up a reliable CFD simulation.

The results provided in this paper have been obtained using regular waves having the same constant steepnessIn future work, it would be interesting to study the variations in fidelity related to independent variations of wave height and period. Furthermore, with the availability of adequate computing resources, more CFD simulations will be carried out in order to provide an accuracy benchmark for different wave conditions.

VI. Conclusion

This paper analyzed the performance of six different nonlinear numerical models for heaving point absorbers. Two main conclusions can be drawn: firstly, nonlinearities are likely to be significant *only* under controlled conditions and, secondly, the most appropriate numerical model is *application specific*, so it depends on accuracy and computational cost requirements, as well as the shape of the device, the implemented control strategy and wave conditions.

Acknowledgment

This paper is based upon work supported by Science Foundation Ireland under Grant No. 13/IA/1886.

References

[1] W. Cummins, "The impulse response function and ship motion," *Schiffstechnik*, no. 9, pp. 101–109, 1962.

[2] W. Inc., *WAMIT v7.0 manual*, 2013.

[3] A. Babarit, H. Mouslim, A. Clément, and P. Laporte-Weywada, "On the numerical modelling of the non linear behaviour of a wave energy converter," in *ASME 2009 28th International Conference on Ocean, Offshore and Arctic Engineering*. American Society of Mechanical Engineers, 2009, pp. 1045–1053.

[4] M. Peñalba, A. Merigaud, J. C. Gilloteaux, and J. V. Ringwood, "Nonlinear Froude-Krylov force modelling for two heaving wave energy point absorbers," in *Proceedings of European Wave and Tidal Energy Conference, Nantes, France*, 2015.

[5] G. Giorgi and J. V. Ringwood, "Implementation of latching control in a numerical wave tank with regular waves," *Journal of Ocean Engineering and Marine Energy*, vol. 2, no. 2, pp. 211–226, 2016.

[6] J.-C. Gilloteaux, "Mouvements de grande amplitude d'un corps flottant en fluide parfait. application à la récupération de l'énergie des vagues." Ph.D. dissertation, Ecole Centrale de Nantes-ECN, 2007.

[7] M. A. Bhinder, A. Babarit, L. Gentaz, and P. Ferrant, "Effect of viscous forces on the performance of a surging wave energy converter," in *Proceedings of the 22nd International and Polar Engineering Conference, Rhodes, Grece*, June 17-22 2012, pp. 545–549.

[8] M. Peñalba, G. Giorgi, and J. V. Ringwood, "A review of non-linear approaches for wave energy converter modelling," in *Proceedings of European Wave and Tidal Energy Conference, Nantes, France*, 6-11 September 2015.

[9] G. Giorgi, M. Penalba, and J. V. Ringwood, "Nonlinear hydrodynamic force relevance for different wave energy converter types," in *3rd Asian Wave and Tidal Energy Conference*, 24-28 October 2016.

[10] K. Budal, J. Falnes, A. Kyllingstad, and G. Oltedal, "Experiments with point absorbers," in *Proceedings of First Symposium on Wave Energy Utilization, Gothenburg, Sweeden*, 1979, pp. 253–282.

[11] J. Newman, *Marine Hydrodynamics*. MIT Press, 1977.

[12] A. Merigaud, J.-C. Gilloteaux, and J. V. Ringwood, "A nonlinear extension for linear boundary element methods in wave energy device modelling," in *ASME 2012 31st International Conference on Ocean, Offshore and Arctic Engineering*. American Society of Mechanical Engineers, 2012, pp. 615–621.

[13] R. Taghipour, T. Perez, and T. Moan, "Hybrid frequency-time domain models for dynamic response analysis of marine structures," *Ocean Engineering*, vol. 35, no. 7, pp. 685–705, May 2007.

[14] D. I. Forehand, A. E. Kiprakis, A. J. Nambiar, and A. R. Wallace, "A fully coupled wave-to-wire model of an array of wave energy converters," *Sustainable Energy, IEEE Transactions on*, vol. 7, no. 1, pp. 118–128, 2016.

[15] G. Giorgi and J. V. Ringwood, "Computationally efficient nonlinear froude-krylov force calculations for heaving axisymmetric wave energy point absorbers," *accepted by Journal of Ocean Engineering and Marine Energy*, 2016.

[16] K. Lok, T. Stallard, P. Stansby, and N. Jenkins, "Optimisation of a clutch-rectified power take off system for a heaving wave energy device in irregular waves with experimental comparison," *International Journal of Marine Energy*, vol. 8, pp. 1–16, 2014.

[17] M. A. Bhinder, A. Babarit, L. Gentaz, and P. Ferrant, "Assessment of viscous damping via 3d-cfd modelling of a floating wave energy device," in *Proceedings of the 9th European Wave and Tidal Energy Conference, Southampton, UK*, 2011.

[18] G. H. Keulegan and L. H. Carpenter, *Forces on cylinders and plates in an oscillating fluid*. US Department of Commerce, National Bureau of Standards, 1956.

[19] B. Molin, *Hydrodynamique des structures offshore*. Editions Technip, 2002.

[20] OpenFOAM, *OpenFOAM The Open Source CFD Toolbox User Guide Version 3.0.1*, 13th December 2015.

[21] R. Temam, *Navier-Stokes equations: theory and numerical analysis*. American Mathematical Soc., 2001, vol. 343.

[22] "Corpower ocean ab, available at http://www.corpowerocean.com/."

[23] "Wavestar a/s, available at http://wavestarenergy.com/."

[24] "Carnegie wave energy limited, available at http://carnegiewave.com/."

[25] B. L. Mehaute, *An Introduction to Hydrodynamics and Water Waves*. Springer, 1976.

[26] R. H. Hansen and M. M. Kramer, "Modelling and control of the wavestar prototype," *Proceedings of the 11th European Wave and Tidal Energy Conference, Southampton, UK*, 2011.

[27] F. d. O. António, "Phase control through load control of oscillating-body wave energy converters with hydraulic pto system," *Ocean Engineering*, vol. 35, no. 3, pp. 358–366, 2008.